Stability and accuracy analysis of approximate deconvolution discretization for non-periodic domains

L. Caban*, A. Tyliszczak*, A. Boguslawski*, S. Stolz**, and B. J. Geurts**,***
Corresponding author: lena.caban@pcz.pl
* Czestochowa University of Technology, Poland.
** University of Twente, The Netherlands.
*** Eindhoven University of Technology, The Netherlands.

Abstract: This paper focuses on the development and analysis of the Approximate Deconvolution Discretization (ADD) method for the numerical solution of fluid-flow problems. The proposed approach builds upon the ADD framework introduced by Boguslawski et al. (Boguslawski A., Tyliszczak A., Geurts B., Approximate Deconvolution Discretisation, Computers and Mathematics with Applications, 154:175–198, 2024) for periodic boundary conditions. The ADD methodology relies on identifying the filter G implicitly induced by a discrete approximation of the derivative operator ($\partial \rightarrow \delta$) and subsequently reversing its effect, to recover part of the information lost through numerical discretization. To extend the ADD framework to non-periodic domains, the induced filter is represented as a superposition of top-hat filters integrated using Lagrange interpolation. Since G is non-singular, its inverse can be computed directly and applied to the discrete derivative operators, yielding $G^{-1}\delta \approx \partial$. Stability analysis shows that the discrete operator $G^{-1}\delta$ is unstable for hyperbolic problems and only conditionally stable for parabolic problems, with stability depending on the level of dissipation and mesh density. To address this issue, a stabilization procedure is proposed that introduces a trade-off between stability and accuracy. The ADD method has been implemented in existing 2D and 3D flow solvers, demonstrating that it can serve as a general framework for enhancing the accuracy of legacy codes. The correctness and effectiveness of the proposed approach are demonstrated using several classical benchmark problems, including the inviscid convected vortex, Burggraf flow, dipole-wall interaction, and lid-driven cavity flow.

Keywords: Approximate deconvolution discretization, High-order schemes, Stability analysis

1. Introduction

Numerical approximations of spatial derivatives inherently introduce discretization errors by replacing continuous differential operators with their discrete counterparts. These discrete operators can be interpreted as exact derivatives acting on filtered representations of the solution, where the filter is implicitly induced by the numerical scheme. This interpretation was first established for a second-order central finite difference approximation of the first derivative, showing that the discrete derivative operator can be represented as the exact derivative of a top-hat filtered field [1]. Geurts and van der Bos [2] later extended this framework to general finite difference and upwind schemes by deriving their corresponding induced filters as superpositions of top-hat filters. Despite their unavoidable presence, numerically induced filters are often neglected in practical simulations because their exact form depends on the applied discretization and, in more complex algorithms, may result from a combination of derivative approximations, interpolation procedures, and time integration effects. Recently, Caban et al. [3] demonstrated that numerically induced filters can significantly affect both the stability and accuracy of approximate-deconvolution-based large-eddy simulations. These findings indicate that discretization-induced filtering is not merely a theoretical consequence of numerical approximation, but can directly affect the predictive capabilities of numerical simulations, particularly in Computational Fluid Dynamics (CFD), with applications spanning a wide range of scales.

Based on the induced filter formalism developed in [2], Boguslawski et al. [4] proposed the Approximate Deconvolution Discretization (ADD) method to compensate for discretization-induced filtering effects. ADD recovers attenuated solution scales through an approximate inversion of the numerically induced filter. This approach provides a largely non-intrusive way for enhancing existing low-order discretization methods without requiring substantial modifications to legacy CFD codes. The original ADD formulation was implemented and illustrated for problems with periodic boundary conditions. In this paper, we extend this to more general problems involving non-periodic boundaries.

A key remaining challenge for the practical deployment of ADD is the treatment of physically relevant boundaries, including inlet/outlet and walls. Extending ADD to these types of boundary conditions is non-trivial because constructing induced filters and their approximate inverses becomes considerably more difficult when stencil support is truncated or asymmetric near boundaries, and periodicity assumptions are no longer valid. Moreover, it turns out that incorporating boundary-specific induced filters and their approximate inverses into the ADD framework may introduce numerical instabilities. An important question is therefore whether the influence of these instabilities can be controlled and remains confined to the vicinity of physical boundaries or affects dynamically important flow structures in the interior of the computational domain. Addressing this issue constitutes one of the objectives of the present work.

In particular, we extend the ADD framework to non-periodic domains and investigate stability and accuracy of the resulting numerical schemes in a hierarchy of two- and three-dimensional benchmark problems, including inviscid vortex advection, Burggraf flow, dipole-wall interaction, and the three-dimensional lid-driven cavity flow. Particular attention is devoted to understanding the practical impact of boundary-induced instabilities and to determining under which flow conditions the substantial accuracy gains provided by ADD can be preserved in non-periodic domains.

The organization of this paper is as follows. In Section 2 we introduce the approximate deconvolution discretization. Section 3 is devoted to a stability analysis of the ADD approach for hyperbolic problems with non-periodic boundaries. In Section 4 we formulate mathematical models in 2D and 3D. Concrete cases for well-known benchmark problems are presented in Section 5, illustrating the improvements in accuracy that are achievable within the ADD uplifting of basic legacy discretizations. Concluding remarks are collected in Section 6.

2. Approximate deconvolution discretization

2.1 General ADD formulation

The general idea of ADD is to compensate *a priori* for the induced filtering effect introduced by numerical discretization. In general, the ADD approximation of the rth order derivative of a function f, evaluated at grid node x_i with $f_i = f(x_i)$, is defined as follows

$$D^{(r)} f_i \equiv Q^{(r)} * \left(\delta^{(r)} f_i\right) = Q^{(r)} * \left(G^{(r)} * \left(\partial^{(r)} f_i\right)\right) \approx \partial^{(r)} f_i \tag{1}$$

where $Q^{(r)} \approx \left[G^{(r)}\right]^{-1}$ denotes the approximate inverse of the filter $G^{(r)}$ induced by the numerical discretization scheme $\delta^{(r)}$. Here, $D^{(r)}$ denotes the ADD-modified approximation of the rth derivative. The equality in (1) follows from the identity $\delta^{(r)} = G^{(r)}\partial^{(r)}$, which relates the discrete derivative to the exact derivative acting on the induced filter [2–4]. The approximation arises because $Q^{(r)}$ represents only an approximate inverse of $G^{(r)}$. For the exact inverse filter, Eq. (1) would recover the exact derivative. Here, we assume that $Q^{(r)}$ and $G^{(r)}$ commute with the partial derivative as well as with each other.

For periodic domains, the same discretization stencil is applied at each computational node, resulting in a spatially invariant induced filter. In such cases, the inverse filter can be efficiently constructed using either Fourier-based techniques or an iterative van Cittert deconvolution [5]. However, in non-periodic domains, the differentiation stencil changes near boundaries, making the induced filter spatially dependent and preventing the direct application of the filter construction proposed in [4]. The restriction to periodic domains constitutes one of the principal limitations of the original ADD formulation. To address this issue, we introduce below a procedure for constructing induced filters in the presence of physical boundaries.

2.2 Extension to non-periodic domains

Consider a uniform 1D grid on the interval $[0, L]$ with K nodes $x_i = h(i-1)$, $i = 1, .., K$, and the mesh spacing $h = L/(K-1)$. A general finite difference (FD) approximation of the first-order derivative can be written as

$$\delta^{(1)} f_i = \frac{1}{h} \sum_{j=-n_b}^{m_b} a_{i,j} f_{i+j} \tag{2}$$

For interior nodes sufficiently far from the boundaries, the derivative is evaluated using a fixed discretization stencil $[-n, m]$, where n and m denote the number of nodes to the left and right of x_i, respectively. Near the boundaries, the stencil is locally adjusted through n_b and m_b to avoid exceeding the computational domain while preserving the total stencil width. In other words, the stencil is progressively shifted toward the interior of the domain as the boundary is approached, which leads to the following definitions of n_b and m_b

$$\begin{array}{rcc} n_b = i-1,\ m_b = m+n+1-i & \text{for} & i = 1, .., n-1 \\ n_b = n,\ m_b = m & \text{for} & i = n, ..., K-m \\ n_b = K+m+n-i,\ m_b = K-i & \text{for} & i = K+1-m, ..., K \end{array} \tag{3}$$

This construction preserves the formal order of accuracy throughout the domain. Following Geurts and van der Bos [2], the induced filter related to the FD scheme (2) can be represented as a weighted superposition of top-hat filters of width h

$$G^{(1)} f_i = \sum_{j=-n_b+1}^{m_b} b_{i,j} \left(\frac{1}{h} \int_{x_i-(j-1)h}^{x_i+jh} f(\eta) d\eta \right) \tag{4}$$

where

$$b_{i,j} = \sum_{i=j}^{m_b} a_{i,j} \quad \text{for} \quad j = -n_b+1, ..., m_b \tag{5}$$

For periodic domains, the induced filter can be constructed using a fixed interpolation stencil. However, in non-periodic domains, the presence of physical boundaries requires local adjustment of this stencil. In the present work, the top-hat integrals appearing in Eq. (4) are approximated using local Lagrange interpolation polynomials, yielding

$$G^{(N^L,M^L)} f_i = \frac{1}{h} \sum_{j=-n_b+1}^{m_b} b_{i,j} \left(\int_{x_i-(j-1)h}^{x_i+jh} f(\eta) d\eta \right) \approx \frac{1}{h} \sum_{j=-n_b+1}^{m_b} b_{i,j} \int_{(j-1)h}^{jh} L_i(\xi) d\xi \tag{6}$$

where $L_i(\xi) = \sum\limits_{k=-N^L}^{M^L} f_{i+k} l_k(\xi)$ denotes the local Lagrange polynomial constructed on an interpolation stencil $[-N^L, M^L]$ containing N^L nodes to the left and M^L nodes to the right of node x_i and $l_k(\xi)$ are the Lagrange polynomial basis. Near the boundaries, N^L and M^L are adjusted such that $N^L + M^L =$ const at each node, which preserves the formal interpolation order. In the present study, a symmetric interpolation stencil is adopted in the interior of the domain, i.e., $N^L = M^L$. After evaluating the integrals in Eq. (6), the resulting induced filter can be expressed in matrix form as $\mathbf{G}^{(1)} = [G_{i,j}]$.

Provided that $\mathbf{G}^{(1)}$ is non-singular, the corresponding deconvolution operator is defined as

$$\mathbf{Q}^{(1)} = \left[\mathbf{G}^{(1)}\right]^{-1} \tag{7}$$

The present study focuses on the first-derivative operator and a particular second-order finite-difference scheme. Nevertheless, the proposed construction is sufficiently general and is not restricted to this specific choice. In principle, the same procedure may be applied to other discretization schemes and to derivative operators of different orders, provided that the corresponding induced filters can be identified.

2.3 Numerical implementation

A second-order finite-difference scheme (FD2) is selected as the baseline discretization because it represents a class of low-order methods widely used in existing CFD solvers. The corresponding first-derivative operator $\delta^{(1)}$, consisting of a central discretization in the interior of the domain and one-sided forward/backward discretizations at the boundaries, can be expressed in matrix form as

$$\mathbf{D}^{(1)}_{\mathrm{FD2}} = [a_{i,j}]/h \tag{8}$$

where the coefficients are given by

- $a_{1,1} = -\frac{3}{2}, a_{1,2} = 2, a_{1,3} = -\frac{1}{2}$
- $a_{i,i-1} = -\frac{1}{2}, a_{i,i} = 0, a_{i,i+1} = \frac{1}{2}$ for $i = 2, ..., K-1$
- $a_{K,K-2} = \frac{1}{2}, a_{K,K-1} = -2, a_{K,K} = \frac{3}{2}$

The resulting ADD-modified derivative operator is then obtained as

$$\mathbf{D}^{(1)} = \mathbf{Q}^{(1)}\mathbf{D}^{(1)}_{\mathrm{FD2}} \tag{9}$$

which is used in all subsequent computations.

To isolate the stability properties of the proposed ADD formulation, deconvolution is applied only to the first-derivative operator $\mathbf{D^{(1)}}$. The second-derivative operator $\mathbf{D^{(2)}}$ is approximated using a stable sixth-order compact finite difference discretization [6] and is not modified by the ADD procedure.

3. Stability analysis

Stability analysis methods for PDEs are comprehensively discussed in the literature, see e.g. [7–9]. Among them, the spectral analysis of semi-discrete operators provides a convenient tool for assessing the stability properties of spatial discretizations. In the present work, the eigenvalue spectra of semi-discrete operators corresponding to the model problems $\frac{\partial u}{\partial t} = \frac{\partial u}{\partial x}$ ($\frac{\mathrm{d}\mathbf{u}}{\mathrm{d}t} = \mathbf{D^{(1)}u}$) and $\frac{\partial u}{\partial t} = \frac{\partial^2 u}{\partial x^2}$ ($\frac{\mathrm{d}\mathbf{u}}{\mathrm{d}t} = \mathbf{D^{(2)}u}$) are analyzed. The semi-discrete operators are considered stable if their eigenvalue spectra satisfy the following conditions: (I) for $\mathbf{D^{(1)}}$, all eigenvalues have non-positive real parts, i.e., $\Re(\lambda_i) \leq 0$ for every eigenvalue λ_i; (II) for $\mathbf{D^{(2)}}$, all eigenvalues are real and non-positive. The stability properties of the proposed ADD-enhanced first-derivative operators are examined below using criterion (I).

Figure 1a shows the eigenvalue spectra of the ADD-modified first-derivative operator $\mathbf{D}^{(1)}$ for different Lagrange interpolation stencils N^L. For $N^L = 1$, all eigenvalues lie in the left half-plane, indicating that the corresponding operator satisfies criterion (I). However, for $N^L \geq 2$, eigenvalues with positive real parts appear, indicating a loss of stability. Moreover, these unstable eigenvalues move progressively further into the right half-plane as N^L increases. In particular, for $N^L \geq 3$ the spectrum contains a pair of complex-conjugate eigenvalues with very large positive real parts.

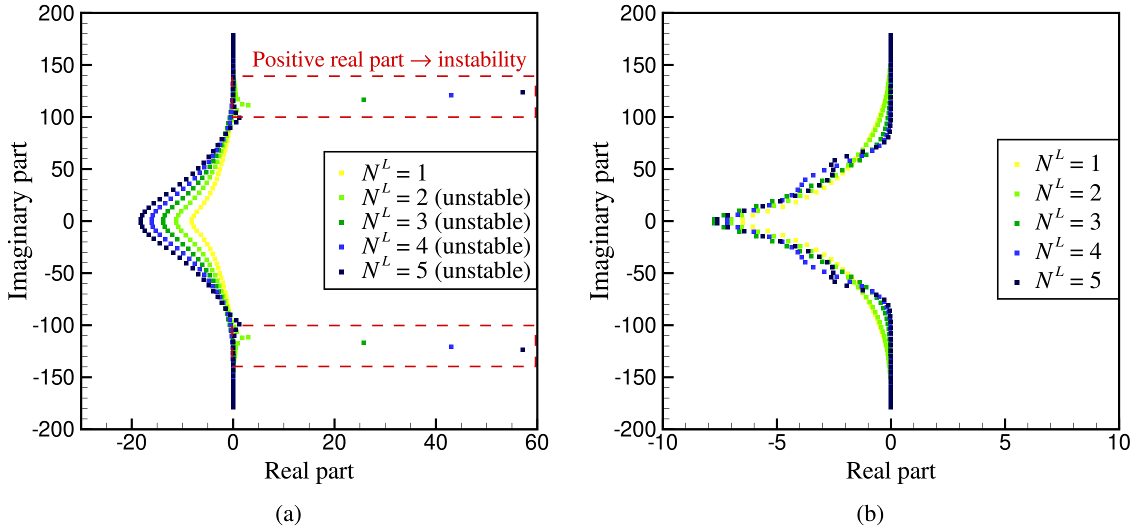

Figure 1: Eigenvalue spectra of first-derivative operators $\mathbf{D}^{(1)}$ (a) and $\mathbf{D}^{(1)}_{\text{mod}}$ (b).

At this point, it should be noted that the definition of solution stability according to criterion (I) does not necessarily determine the behavior of the complete flow solver. For viscous flow problems, the dissipative nature of the governing equations can mitigate the effects of unstable eigenmodes. We will demonstrate that the solution stability depends on mutual interactions between the convective and dissipative forces. Furthermore, we propose a simple solution to eliminate the unstable modes observed in Fig. 1a by modifying the boundary treatment. The idea is to disable the deconvolution procedure at boundary and near-boundary nodes, while maintaining the standard ADD formulation in the interior of the domain. Starting from the induced filter matrix $\mathbf{G}^{(1)} = [G_{i,j}]$, a modified filter matrix $\mathbf{G}^{(1)}_{\text{mod}} = [G^*_{i,j}]$ is constructed by replacing the first and last N^L rows with the corresponding rows of the identity matrix. In other words,

$$G^*_{i,j} = \begin{cases} 1, & i = j \\ 0, & i \neq j \end{cases} \quad \text{for} \quad i = 1, \ldots, N^L \quad \text{and} \quad i = K - N^L + 1, \ldots, K \tag{10}$$

The remaining rows of $\mathbf{G}^{(1)}_{\text{mod}}$ are left unchanged, i.e. $G^*_{i,j} = G_{i,j}$ for $i = N^L + 1, \ldots, K - N^L$. As a result, deconvolution is effectively applied only in the interior of the computational domain, while the original FD2 approximation is retained at the boundary and near-boundary nodes. The corresponding deconvolution operator is defined as

$$\mathbf{Q}^{(1)}_{\text{mod}} = \left[\mathbf{G}^{(1)}_{\text{mod}}\right]^{-1} \tag{11}$$

The resulting stabilized ADD operator is then obtained as

$$\mathbf{D}^{(1)}_{\text{mod}} = \mathbf{Q}^{(1)}_{\text{mod}} \mathbf{D}^{(1)}_{\text{FD2}}. \tag{12}$$

Figure 1b presents the eigenvalue spectra of the stabilized ADD operator $\mathbf{D}^{(1)}_{\text{mod}}$. It can be observed that all eigenvalues remain in the left half-plane for all considered interpolation stencils N^L, indicating that the corresponding operators satisfy criterion (I). This confirms that the proposed boundary treatment effectively eliminates the unstable modes present in the standard ADD formulation. Moreover, compared to Fig. 1a, the spectra of $\mathbf{D}^{(1)}_{\text{mod}}$ are also noticeably compressed along the real axis, which in practice allows one to apply larger time steps. An important aspect of disabling deconvolution near boundaries is the potential reduction in solution accuracy. We will demonstrate that the stabilization procedure introduces a trade-off between stability and ADD's ability to recover solution scales affected by discretization-induced filtering. We will show that this trade-off is problem-dependent, i.e., there are flow problems in which the use of $\mathbf{D}^{(1)}_{\text{mod}}$ may totally deteriorate solution accuracy, and there are also cases in which this effect is negligible. Therefore, both the standard and the stabilized ADD formulations are investigated in the numerical experiments presented in the following sections.

It should be noted that the above analysis concerns only the spatial discretization operators. In practical computations, stability also depends on the time integration method employed through the location of scaled eigenvalues $\Delta t \lambda_i$ within its stability region [10]. As mentioned above, the modified ADD formulation permits the use of larger time steps. Nevertheless, the same time step is used throughout this study for both the classical second-order FD scheme as well as for the standard and stabilized ADD formulations. The chosen time step is sufficiently small for the numerical errors to be dominated by the spatial discretization, as confirmed by additional simulations conducted with smaller time steps.

4. Numerical frameworks

To assess the proposed ADD formulation for non-periodic boundary conditions, we employ both the dimensionless vorticity–stream function formulation and the velocity–pressure formulation of the Navier-Stokes (N–S) equations. The former is used in the two-dimensional benchmark problems, while the latter is considered for the three-dimensional lid-driven cavity flow. In all cases, we consider a non-dimensional framework.

4.1 Two-dimensional formulation

The two-dimensional formulation is based on the vorticity transport equation coupled with the Poisson equation for the stream function

$$\frac{\partial \omega}{\partial t} + u\frac{\partial \omega}{\partial x} + v\frac{\partial \omega}{\partial y} - \frac{1}{\mathrm{Re}}\left(\frac{\partial^2 \omega}{\partial x^2} + \frac{\partial^2 \omega}{\partial y^2}\right) = f \tag{13}$$

where ω is the vorticity, u, v are the velocity components, Re is the Reynolds number and f is a source term. The velocity components are calculated from the stream function ψ ($u = \frac{\partial \psi}{\partial y}$, $v = -\frac{\partial \psi}{\partial x}$) which is obtained from the Poisson equation

$$\frac{\partial^2 \psi}{\partial x^2} + \frac{\partial^2 \psi}{\partial y^2} = -\omega \tag{14}$$

A matrix diagonalization technique of Lynch et al. [11] is used to solve Eq. (14). The second derivatives in this equation and also in Eq. (13) are approximated using the sixth-order stable compact finite difference scheme proposed in [6]. For all 2D benchmark problems considered in the present work, temporal integration is performed using the classical fourth-order Runge-Kutta (RK4) method. The time step is specified individually for each benchmark problem.

4.2 Three-dimensional formulation

The three-dimensional formulation is based on the incompressible Navier-Stokes equations expressed in the velocity–pressure form

$$\frac{\partial u_j}{\partial x_j} = 0 \tag{15}$$

$$\frac{\partial u_i}{\partial t} + u_j\frac{\partial u_i}{\partial x_j} + \frac{1}{\rho}\frac{\partial p}{\partial x_i} - \frac{1}{\mathrm{Re}}\frac{\partial^2 u_i}{\partial x_j^2} = f_i \tag{16}$$

where u_i are the velocity components, ρ is a constant density assumed equal to one, p is the pressure calculated using a projection method [12], and f_i is the i-th component of the external force per unit mass.

The 3D simulations are performed using an in-house SAILOR code [13], which is based on a half-staggered grid arrangement [14]. In this approach, the pressure nodes are shifted by half a mesh spacing relative to velocity nodes. When the ADD method is applied, it acts only on the convective terms in Eq. (16), discretized using the FD2 scheme. When ADD is not applied, either the FD2 scheme, or a compact difference method with variable discretization order is used. In the latter case, the order increases progressively from three near the boundaries to ten in the interior of the domain. The pressure gradient, the continuity equation (15), and the Poisson equation within the projection method are discretized applying a combination of the second- and fourth-order finite difference methods, see [13]. In all cases, the second-derivative in Eq. (16) is approximated by the compact difference scheme of the order changing progressively from three to ten from the boundary to the central nodes. Time integration employs a predictor-corrector scheme combining the second-order Adams-Bashforth and Adams-Moulton methods.

5. Results

The proposed ADD formulation is assessed using a hierarchy of benchmark problems designed to examine both its accuracy and stability in the presence of physical boundaries. The considered test cases include inviscid vortex advection, Burggraf flow, dipole-wall interaction, and a three-dimensional lid-driven cavity flow. Together, these configurations provide a progressive increase in complexity, ranging from a smooth inviscid advection problem with an analytical solution to fully nonlinear viscous flows in confined domains. The inviscid vortex advection case is particularly useful because it isolates the behavior of the ADD-enhanced first-derivative operator, allowing the accuracy of the proposed deconvolution procedure to be assessed independently of viscous effects and second-derivative discretization errors.

The first three test cases are solved using the two-dimensional vorticity–stream function formulation introduced in Section 4.1, whereas the lid-driven cavity flow is computed using the three-dimensional velocity–pressure formulation described in Section 4.2.

5.1 Inviscid vortex advection

We begin the numerical assessment of the proposed ADD formulation with the inviscid vortex advection problem. This test case is a well-established benchmark for evaluating the accuracy of high-order discretization methods, see e.g. [13, 15, 16]. In most previous studies, the problem has been considered on periodic domains. In the present work, however, the computations are performed in a finite domain with physical boundaries, providing a convenient framework for evaluating the behavior of the ADD methodology under non-periodic boundary conditions. Moreover, since the governing equations do not contain diffusive terms, the influence of the second-derivative discretization is eliminated, allowing the performance of the ADD-enhanced first-derivative operator to be assessed in isolation.

The computations are performed in a square domain of size $L_x = L_y = 20$. The vortex is transported in a uniform velocity field ($u_\infty = 1$, $v_\infty = 1$) without deformation. In terms of the velocity components, it is analytically defined as

$$\begin{aligned} u_a(x, y, t) &= u_\infty - C(y - y_c)\exp(-r^2/2) \\ v_a(x, y, t) &= v_\infty + C(x - x_c)\exp(-r^2/2) \end{aligned} \tag{17}$$

Here, $(x_c, y_c) = (x_0 + u_\infty t, y_0 + v_\infty t)$ denotes the position of the vortex center, $(x_0, y_0) = (10, 10)$ is its initial position, and $r = \sqrt{(x - x_c)^2 + (y - y_c)^2}$. The parameter C determines the vortex strength and is set to 0.6944 following [13, 15, 16]. The boundary conditions are time dependent and are defined according to Eq. (17).

Unless otherwise stated, the computations are performed with a time step $\Delta t = 1 \times 10^{-6}$. The numerical error is evaluated using the discrete L_2 error norm defined as

$$\text{Error} = \sqrt{\frac{1}{K_x K_y}\sum_{i=1}^{K_x}\sum_{j=1}^{K_y}\left[u(x_i, y_j, t) - u_a(x_i, y_j, t)\right]^2} \tag{18}$$

where K_x and K_y denote the number of grid points in the x and y directions, respectively.

As an illustration of the flow field, Fig. 2 shows the contours of the velocity components u and v, together with the vorticity ω at time $t = 1$. At this moment, the vortex remains far from the boundary. Thus, the impact of the boundary on the accuracy of calculating the vortex position and its shape is limited.

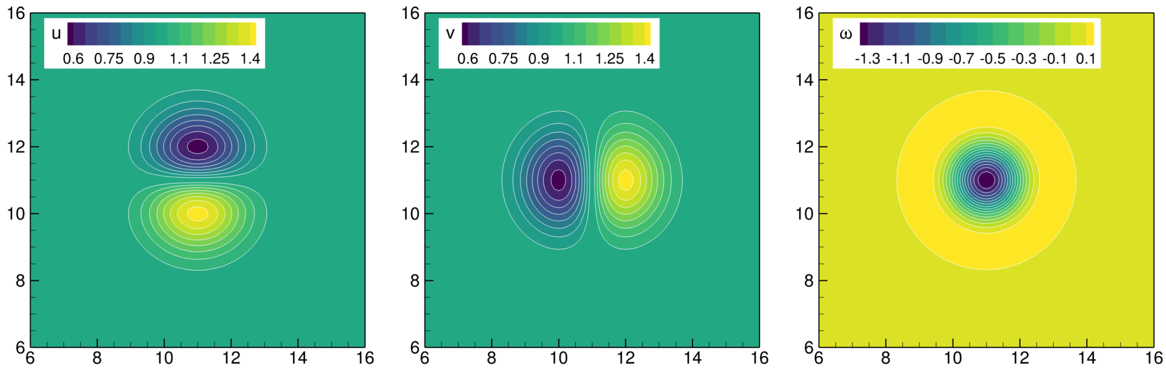

(a) (b) (c)

Figure 2: Inviscid vortex advection: contours of the velocity components u (a) and v (b), and vorticity ω (c) at time $t = 1$ in a central part of the computational domain.

Figure 3 shows the L_2 error norm at $t = 1$ as a function of the number of grid points for the solutions obtained using the FD2 scheme and the ADD-enhanced formulation with various interpolation stencils N^L. The FD2 scheme exhibits the expected second-order convergence, whereas the ADD-enhanced discretization yields significantly lower errors on all considered meshes. For a fixed time step $\Delta t = 1 \times 10^{-6}$, the accuracy systematically improves with increasing interpolation stencil width N^L. However, for $N^L = 4$ and $N^L = 5$, the error eventually reaches a plateau. Additional computations performed with $\Delta t = 1 \times 10^{-8}$ demonstrate that the apparent loss of convergence is caused by temporal discretization errors rather than by the ADD procedure itself. Further reduction of the time step to $\Delta t = 1 \times 10^{-9}$ gives practically identical results, indicating that time integration errors are negligible at this level. These results show that, in the absence of boundary effects, increasing N^L leads to a systematic improvement in solution accuracy.

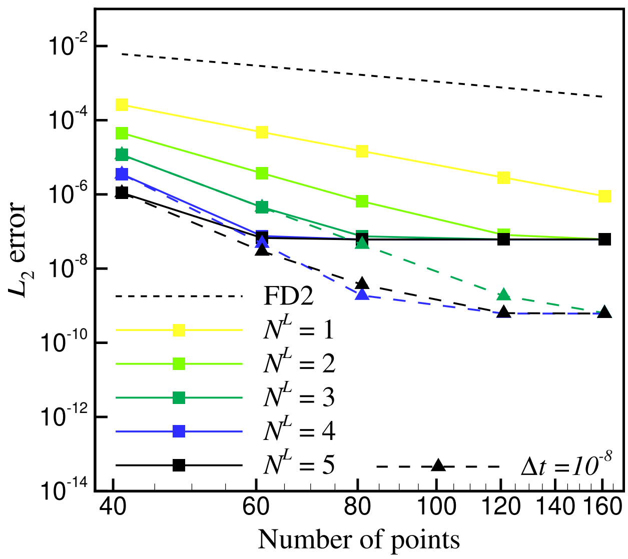

Figure 3: Inviscid vortex advection: L_2 error norm as a function of grid points. Results obtained using the FD2 scheme and standard ADD formulation at $t = 1$.

Regarding the instability problem of the standard ADD method discussed in Section 3, it may seem surprising that, despite being very accurate, the obtained solutions were also stable. The reason for this is a short simulation time ($t = 1$) during which the unstable eigenmodes did not manage to deteriorate the solution. However, their presence ultimately affects long-term behavior. Extending the simulation time revales that the instability occurs progressively later as N^L decreases, appearing at approximately $t \approx 4, 5$, and 7 for $N^L = 5, 4$, and 3, respectively. For sufficiently long integration times, only the stabilized ADD formulation maintains numerical stability. At $t = 5$, it retains the favorable convergence properties shown in Fig. 3 and continues to provide a substantial improvement over the underlying FD2 scheme.

The present results show that the ADD methodology can deliver highly accurate solutions despite the operator-level instabilities identified in Section 3. Moreover, the stabilized formulation retains essentially the same accuracy as the standard ADD approach, while ensuring long-term stability. However, this conclusion is drawn based on the results obtained at the moment when the vortex is still quite far from the boundaries and the variability of the solution in their vicinity is small, $\left(\text{i.e., } u_a\left(\frac{L_x}{2}, \frac{L_y}{2}, 5\right) \approx u_\infty, v_a\left(\frac{L_x}{2}, \frac{L_y}{2}, 5\right) \approx v_\infty\right)$. In the following benchmark problems, viscous effects and near-wall flow dynamics are considered, allowing the analysis of the boundary-induced instabilities identified in Section 3 and the consequences of applying the stabilized ADD formulation.

5.2 Burggraf flow

The first convection-diffusion test case is the regularized shear-driven cavity flow, commonly known as the Burggraf flow. It belongs to a limited class of CFD benchmark problems for which analytical solutions are available and is therefore often used for detailed accuracy assessments of numerical schemes [6, 13, 17]. The flow is considered in a square cavity of size $L_x = L_y = 1$. No-slip boundary conditions are imposed on all walls. The upper wall moves with the prescribed tangential velocity distribution $u(x) = 16(x^4 - 2x^3 + x^2)$, while $v = 0$ along the entire boundary. Figure 4a schematically illustrates the computational domain and boundary conditions, while Figs. 4b and 4c show contours of the vorticity ω and the velocity component u. The flow inside the cavity is driven by a forcing term $f = \frac{\partial f_v}{\partial x}$ introduced in Eq. (13), where f_v has the form

$$f_v(x, y) = -\frac{8}{\text{Re}}\left[24g + 2g''h'' + g^{(4)}h\right] + 64\left[\frac{g'^2}{2}(hh''' - h'h'') - hh'\left(g'g''' - g''^2\right)\right] \tag{19}$$

The symbols g', g'', g''', $g^{(4)}$, h', h'', and h''' denote the derivatives of the functions g and h, where $g(x) = \frac{x^5}{5} - \frac{x^4}{2} + \frac{x^3}{3}$ and $h(y) = y^4 - y^2$. The analytical solution in velocity components is given as

$$u_a(x, y) = 8\left(x^4 - 2x^3 + x^2\right)\left(4y^3 - 2y\right); \quad v_a(x, y) = -8\left(4x^3 - 6x^2 + 2x\right)\left(y^4 - y^2\right) \tag{20}$$

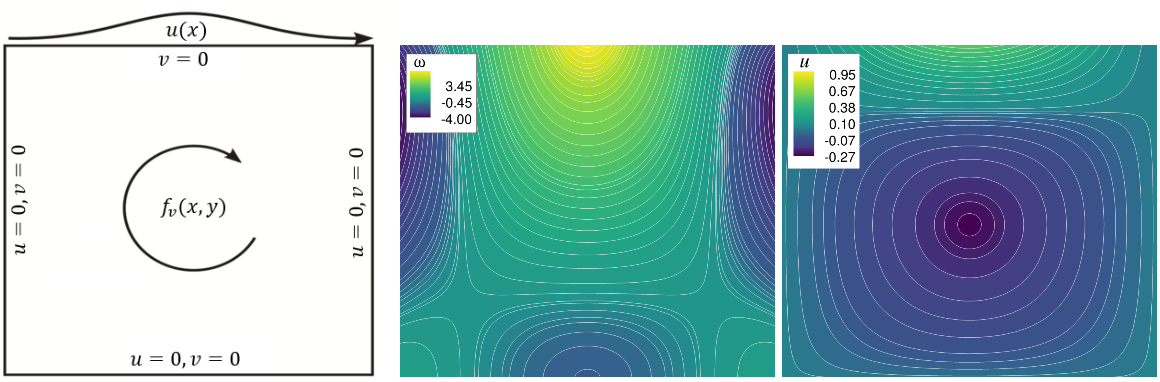

(a) (b) (c)

Figure 4: Burggraf flow: configuration (a), contours of the vorticity ω (b) and u-velocity component (c).

The computations are performed on uniform grids with $K \times K$ nodes, where $K = 41, 61, 81, 121, 161$. Time integration is carried out with a time step $\Delta t = 5 \times 10^{-4}$ and simulations are advanced until a steady state is reached. This is identified by the residual of the vorticity transport equation (13) decreasing to the machine precision level ($\sim 10^{-12}$).

We first consider the standard ADD formulation defined by Eq. (9), despite its operator-level instability discussed in Section 3. Figure 5 presents the results obtained using the basic FD2 scheme and its ADD-enhanced versions. Figure 5a shows the L_2 error of the u-velocity as a function of the number of grid nodes for Re = 1000. Despite the unstable eigenmodes of the first-derivative operator for $N^L \geq 2$, we observe that the solution is stable, and moreover, a significant accuracy improvement is observed compared to the classical FD2 scheme. For $N^L \geq 4$ the solution error reaches the level of the round-off error even on very coarse meshes. The observed stability is attributed to the physical dissipation mechanism discussed earlier, which evidently suppresses the influence of the unstable eigenmodes.

At higher Reynolds numbers, however, the stabilizing effect of physical dissipation becomes less pronounced. Figure 5b shows the temporal evolution of the residual, defined as the RMS of all spatial terms in Eq. (13), for Re = 5000 on a grid with $K = 41$ nodes. For ADD-enhanced discretizations with $N^L \geq 2$, the residual remains nearly constant for a substantial period of time and subsequently exhibits rapid growth. The number of iterations preceding the instability increases as N^L decreases. As in the case of an inviscid vortex advection, this behavior shows that the unstable eigenmodes affect the long-term stability of the computations, not their short-term accuracy.

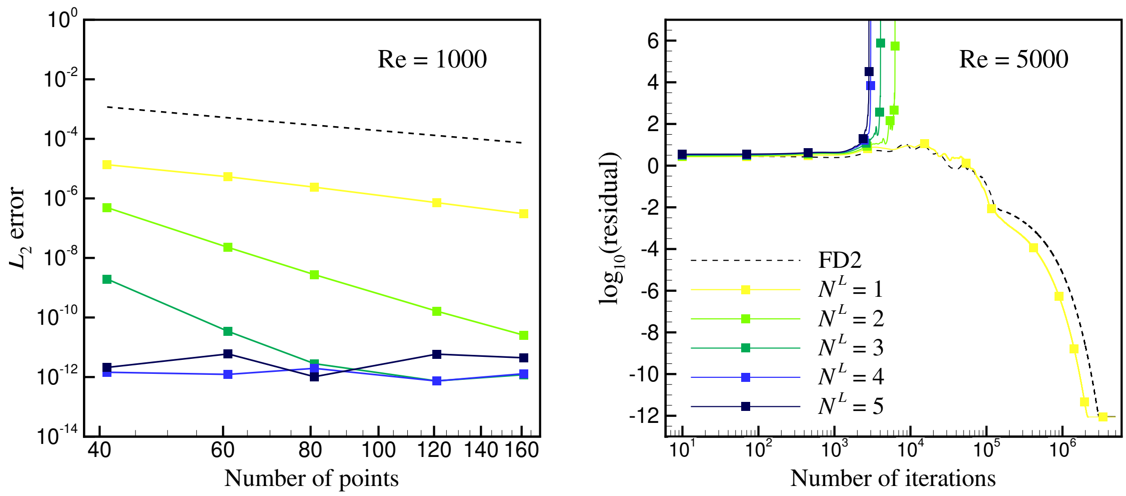

(a) (b)

Figure 5: Burggraf flow: L_2 error norm at Re = 1000 (a). Evolution of the residual for Re = 5000 on the grid with $K = 41$ (b). The legend is the same for both subfigures.

Table 1 reports the L_2 error for Re = 5000 as a function of the grid resolution. While instability is observed on coarse meshes, viscous dissipation on finer grids effectively suppresses the unstable modes, and the obtained solutions demonstrate very high accuracy. For example, on the finest grid ($K = 161$), the FD2 scheme yields an error on the order of 10^{-3}, while the ADD-enhanced formulation reduces it to the order of 10^{-12} (for $N^L = 3$). Assuming second-order convergence of the FD2 scheme, achieving a comparable level of accuracy would require approximately 2×10^6 grid points in each spatial direction. This illustrates the significant increase in accuracy provided by the proposed ADD approach.

It is worth noting that because of the high-order compact difference scheme applied to the viscous term, its discretization error is negligible. It can be seen that the solution accuracy depends on the discretization of the advection terms. However, the inclusion of the former is essential for stability. In their absence, mesh refinement alone does not suppress the instability. We therefore conclude that stabilization results from the combined action of grid refinement and viscous dissipation. The mechanism responsible for

Table 1: Burggraf flow: L_2 error norm of the u-velocity at Re = 5000 obtained using FD2 and ADD-enhanced schemes for different grid resolutions K. Symbol "–" denotes unstable computations.

K	FD2	$N^L = 1$	$N^L = 2$	$N^L = 3$	$N^L = 4$	$N^L = 5$
41	0.13×10^{-2}	0.72×10^{-4}	–	–	–	–
61	0.75×10^{-3}	0.30×10^{-5}	0.22×10^{-6}	–	–	–
81	0.62×10^{-3}	0.39×10^{-5}	0.25×10^{-7}	0.20×10^{-10}	–	–
121	0.29×10^{-3}	0.15×10^{-5}	0.13×10^{-8}	0.23×10^{-11}	0.25×10^{-11}	0.20×10^{-10}
161	0.16×10^{-3}	0.69×10^{-6}	0.17×10^{-9}	0.21×10^{-12}	0.21×10^{-11}	0.24×10^{-10}

this behavior is analogous to the well-known stability criterion of second-order central discretization, expressed in terms of the Peclet number ($Pe \leq 2$) [18]. This issue is beyond the scope of the present study and will be investigated in future work.

Although the standard ADD formulation may exhibit operator-level instability, the above results demonstrate that highly accurate solutions can still be obtained in viscous flows when sufficient dissipation is provided by the governing equations and the computational grid. Nevertheless, from a practical point of view, it is desirable to construct a formulation that satisfies the stability criterion (I) introduced in Section 3. For this purpose, the stabilized ADD operator defined by Eq. (12) is considered next.

Figure 6 shows the results obtained using the stabilized ADD formulation for both Reynolds numbers, Re = 1000 and Re = 5000. In contrast to the standard ADD operator, all computations remain stable for all considered interpolation stencils and grid resolutions. However, the significant accuracy improvement observed for the standard ADD formulation is almost entirely lost. The error levels obtained with the stabilized operator remain close to those obtained using the classical FD2 scheme, indicating that disabling deconvolution near the boundaries significantly weakens the corrective effect of ADD. This suggests that the impact of the modified boundary treatment may depend on the relative importance of near-boundary regions in the overall flow dynamics. In the inviscid vortex advection problem, where the vortex remains sufficiently far from the physical boundaries, the stabilized ADD formulation retained essentially the same level of accuracy as the standard ADD approach. In contrast, the Burggraf flow is strongly influenced by wall boundary conditions throughout the domain, making the effects of the modified boundary treatment much more pronounced.

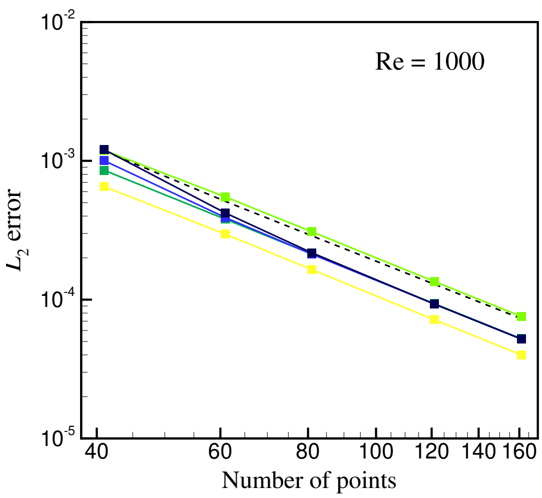

(a)

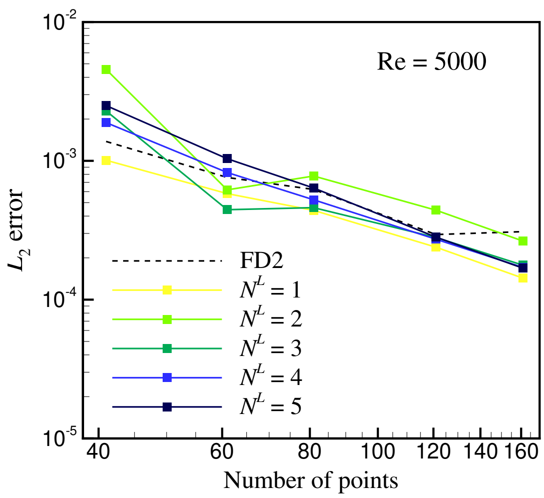

(b)

Figure 6: Burggraf flow: L_2 error norm of the u-velocity obtained using the stabilized ADD formulation for Re = 1000 (a) and Re = 5000 (b). The legend is the same for both subfigures.

5.3 Dipole-wall interaction

The dipole-wall interaction problem is considered as a third representative test case. It provides a demanding benchmark for assessing the proposed ADD formulation in unsteady wall-bounded flows. In contrast to the Burggraf flow, this case involves strong convection, rapid generation of thin boundary layers, and the formation of small-scale vortical structures during the collision process. As shown by Clercx and Bruneau [19], accurate numerical simulation of this problem is particularly challenging due to the strong sensitivity of the flow evolution to near-wall vorticity production and subsequent vortex-wall interactions. Moreover, obtaining grid-independent solutions for this problem remains difficult [19].

The present configuration follows the normal dipole-wall collision benchmark proposed in [19]. The flow is solved in a square domain of size $L_x = L_y = 2$ with no-slip boundary conditions imposed on all walls. The initial condition consists of a dipole formed by a pair of counter-rotating vortices. The initial vorticity distribution is defined as $\omega_{1,2}(x, y, 0) = \pm\omega_e(1 - (r_{1,2}/r_0)^2)\exp(-(r_{1,2}/r_0)^2)$, where $r_{1,2}$ denotes the distance from the vortex centers located at (x_1, y_1) and (x_2, y_2), i.e., $r_1 = \sqrt{(x - x_1)^2 + (y - y_1)^2}$, $r_2 = \sqrt{(x - x_2)^2 + (y - y_2)^2}$, and r_0 is the vortex radius. The parameter ω_e denotes the extremum of vorticity at $r_{1,2} = 0$. In the present simulations, the vortex centers are located at $(x_1, y_1) = (1.0, 1.1)$ and $(x_2, y_2) = (1.0, 0.9)$, with $r_0 = 0.1$. The initial conditions for the velocity components are given by

$$\begin{aligned} u(x, y, 0) &= -\frac{1}{2}\omega_e(y - y_1)\exp(-(r_1/r_0)^2) + \frac{1}{2}\omega_e(y - y_2)\exp(-(r_2/r_0)^2) \\ v(x, y, 0) &= +\frac{1}{2}\omega_e(x - x_1)\exp(-(r_1/r_0)^2) + \frac{1}{2}\omega_e(x - x_2)\exp(-(r_2/r_0)^2) \end{aligned} \tag{21}$$

The vorticity amplitude $\omega_e \approx 300$ is adjusted such that the initial kinetic energy

$$E(t) = \frac{1}{2}\int_0^2\int_0^2 (u(x, y, t)^2 + v(x, y, t)^2)\mathrm{d}x\mathrm{d}y \tag{22}$$

is equal to $E(0) = 2$. This initialization ensures that both velocity and vorticity remain negligible near the boundaries at $t = 0$, thereby avoiding artificial boundary layer generation [19]. The numerical results are assessed through the temporal evolution of the enstrophy $\Omega(t)$ and palinstrophy $P(t)$, defined as

$$\Omega(t) = \frac{1}{2}\int_0^2\int_0^2 \omega(x, y, t)^2\mathrm{d}x\mathrm{d}y, \quad P(t) = \frac{1}{2}\int_0^2\int_0^2 (\nabla\omega(x, y, t))^2\mathrm{d}x\mathrm{d}y \tag{23}$$

Both quantities are highly sensitive to the generation of small-scale vorticity structures and are therefore widely used as diagnostic measures in dipole-wall interaction studies.

The computations are performed for Reynolds numbers Re = 625 and Re = 1250. Reference solutions are generated using the Chebyshev pseudo-spectral (PS) method. For Re = 625, the PS solution is obtained on a non-uniform grid with $K = 257$ Gauss-Lobatto nodes, while the FD2 and ADD methods are tested on uniform grids ranging from $K = 257$ to 1025. For Re = 1250, the PS reference solution is computed on $K = 385$ Gauss-Lobatto nodes, whereas the FD2 and ADD methods are evaluated on uniform grids ranging from $K = 769$ to $K = 1025$. The finest FD grids are selected to enable direct comparison with the benchmark results of Clercx and Bruneau [19]. A summary of all considered methods, grid resolutions, and comparison metrics is provided in Tables 2 and 3.

For the present PS reference simulations, the time step is set to $\Delta t = 2 \times 10^{-6}$ for Re = 625, and $\Delta t = 1 \times 10^{-6}$ for Re = 1250. All remaining FD2 and ADD simulations, regardless of the grid resolution and Reynolds number, are performed with a time step of $\Delta t = 1 \times 10^{-5}$. Additional computations performed with $\Delta t = 2 \times 10^{-6}$ and $\Delta t = 1 \times 10^{-6}$, produce indistinguishable results, indicating that temporal discretization errors are negligible compared to spatial discretization errors.

The obtained results are compared with the present PS reference solutions, the PS and FD results reported by Clercx and Bruneau [19], and the Variant 1_{HO} and Variant 1_{LO} results obtained using the high-order compact difference (HOCD) method reported by Tyliszczak [13]. These two HOCD variants differ in the discretization of the pressure Poisson equation, while both employ high-order compact difference spatial discretizations. It should also be noted that the finite difference method used in Ref. [19] is a combination of the third-order upwind method and the FD2 scheme. Thus, it differs from the FD2 scheme adopted in the present work. Given the variety of literature solutions, the ADD methodology for this test case is assessed against both classical and high-fidelity numerical discretization approaches widely used in CFD.

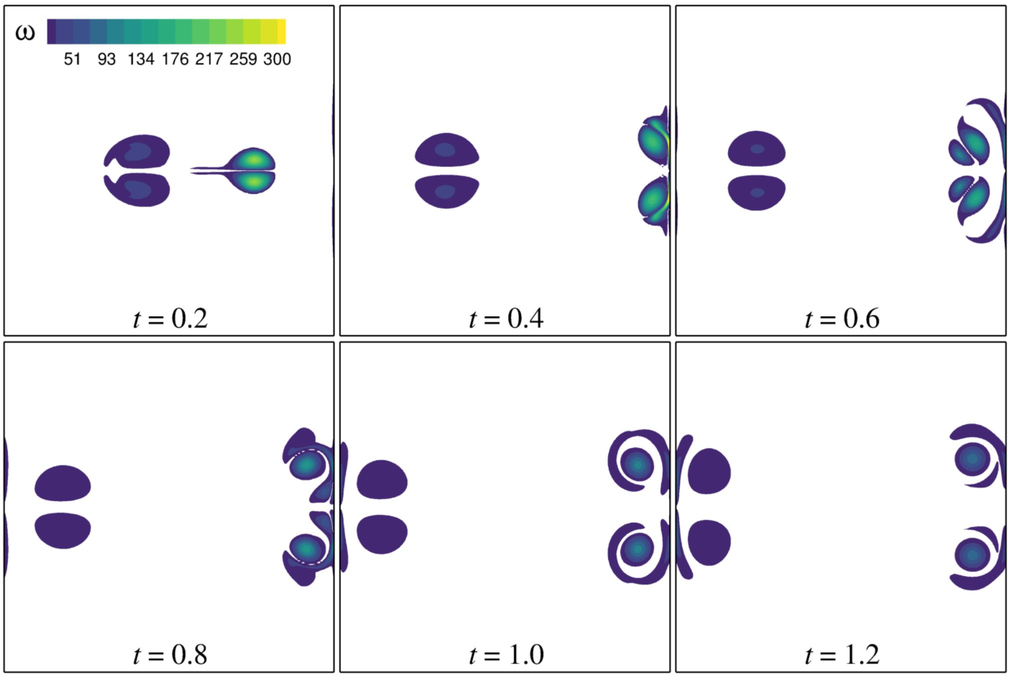

Figure 7: Dipole-wall interaction: vorticity contours at selected time instances for Re = 625.

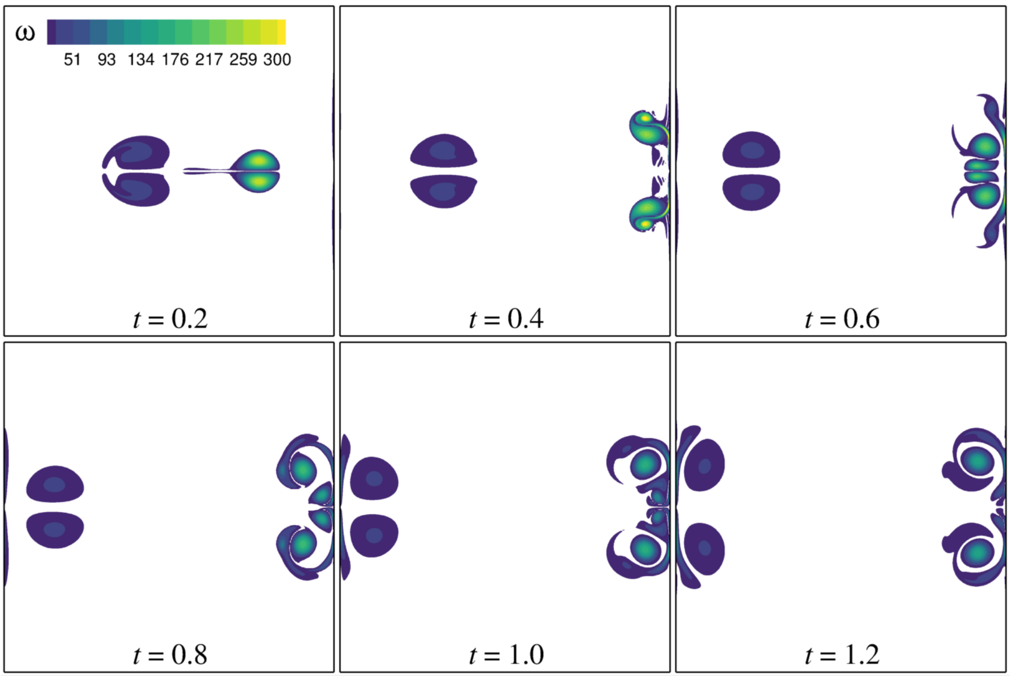

Figure 8: Dipole-wall interaction: vorticity contours at selected time instances for Re = 1250.

We first analyze the PS reference solution to identify the key stages of the dipole-wall interaction process and to characterize the evolution of enstrophy and palinstrophy. Figures 7 and 8 show the evolution of the vorticity field obtained using the PS method for Re = 625 and Re = 1250, respectively. At early times, the dipole remains well separated from the boundaries and maintains its overall structure as it propagates toward the right wall. As the flow evolves, increasingly complex vortical patterns develop due to vortex-wall interaction. These effects are particularly pronounced for Re = 1250, where a larger number of small-scale vortical structures can be observed

The temporal evolution of enstrophy $\Omega(t)$ and palinstrophy $P(t)$ for the PS reference solutions is shown in Figure 9. In both cases, the first pronounced maximum occurs during the initial collision of the dipole with the right wall at approximately $t \approx 0.4$, followed by a second maximum at later times. The amplitudes of both maxima increase with Reynolds number, reflecting the stronger vorticity gradients and more intense small-scale flow structures observed at Re = 1250. Tables 2 and 3 summarize the values and occurrence times of the first and second maxima of enstrophy and palinstrophy. The present PS reference solutions show excellent agreement with the benchmark PS results of Clercx and Bruneau [19], reproducing both the amplitudes and occurrence times of the extrema with virtually identical accuracy for both Reynolds numbers. This comparison provides an independent validation of the present PS implementation and establishes a reliable reference for assessing the FD2 and ADD discretizations.

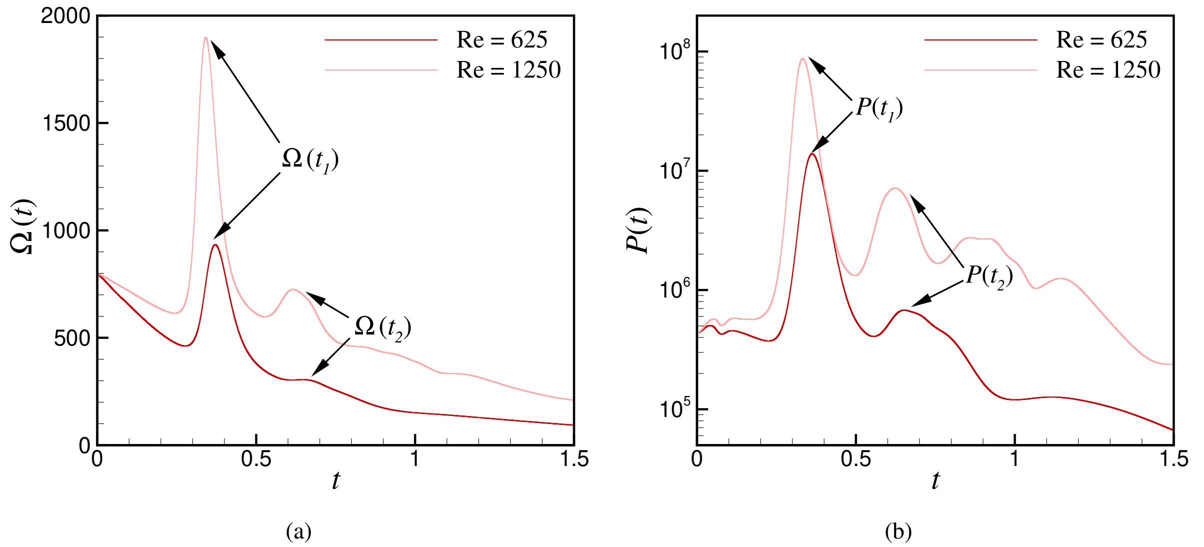

Figure 9: Dipole-wall interaction: time evolution of enstrophy (a) and palinstrophy (b) obtained using the PS reference solutions.

Having established the accuracy of the PS reference solutions, we assess the performance of the FD2 and ADD-enhanced discretization. First, we note that for both Reynolds numbers considered in this benchmark, the standard ADD formulation remains stable. In this test case, an additional factor that may lead to a stable solution is that the flow energy decreases over time. This may also apply to unstable modes, preventing them from unbounded growth. Consequently, the use of the stabilized ADD operator introduced in Section 3 is unnecessary. Figures 10 and 11 compare the temporal evolution of enstrophy and palinstrophy obtained using the FD2 and ADD-enhanced discretizations against the PS reference solution for Re = 625. On the coarse grid with $K = 257$ (Figs. 10a and 11a), the FD2 scheme significantly underpredicts the extrema of both quantities. The ADD-enhanced discretizations substantially improve the prediction of extrema, although no systematic trend with increasing N^L is evident. On the finer grid with $K = 513$ (Figs. 10b and 11b), all methods yield results that are considerably closer to the PS reference solution. While the differences between the individual ADD variants become smaller, a clear ordering with respect to N^L is still not observed. For comparison, literature data are additionally reported in Tables 2 and 3.

Table 2: The values of the first two maxima of enstrophy for Re = 625 and Re = 1250.

Re	Results	K	t_1	$\Omega_1(t_1)$	t_2	$\Omega_2(t_2)$
625	PS	257	0.3711	933.4	0.6479	305.2
	PS [19]	256	0.3711	933.6	0.6479	305.2
	FD2	257	0.3793	678.7	0.6721	268.7
		513	0.3762	867.8	0.6457	301.3
		769	0.3728	915.3	0.6464	303.8
		1025	0.3718	926.0	0.6475	304.4
	FD [19]	1025	0.371	932.8	0.647	305.2
	$N^L = 1$	257	0.3840	709.9	0.6830	284.4
	$N^L = 2$	257	0.3827	791.1	0.6554	295.3
	$N^L = 3$	257	0.3808	817.4	0.6365	297.9
	$N^L = 4$	257	0.3790	803.5	0.6309	297.5
	$N^L = 5$	257	0.3777	773.4	0.6390	296.9
	$N^L = 1$	513	0.3746	907.1	0.6496	304.8
	$N^L = 2$	513	0.3739	909.4	0.6476	305.5
	$N^L = 3$	513	0.3739	901.7	0.6487	305.0
	$N^L = 4$	513	0.3742	897.3	0.6495	304.8
	$N^L = 5$	513	0.3745	897.1	0.6493	304.8
	$N^L = 1$	769	0.3721	930.8	0.6484	305.1
	$N^L = 2$	769	0.3719	929.9	0.6484	305.2
	$N^L = 3$	769	0.3720	928.6	0.6486	305.0
	$N^L = 4$	769	0.3720	929.2	0.6486	305.1
	$N^L = 5$	769	0.3721	930.1	0.6486	305.1
	Variant I_{HO} [13]	512	0.3736	883.1	0.6514	303.2
		768	0.3720	923.2	0.6486	304.9
		1024	0.3714	931.7	0.6480	305.1
1250	PS	385	0.3414	1898	0.6162	725.4
	PS [19]	384	0.3414	1899	0.6162	725.3
	FD2	769	0.3462	1703	0.6148	708.9
	FD2	1025	0.3436	1819	0.6150	718.1
	FD [19]	1536	0.341	1891	0.616	724.9
	$N^L = 1$	769	0.3449	1816	0.6160	724.5
	$N^L = 2$	769	0.3442	1827	0.6147	724.5
	$N^L = 3$	769	0.3442	1805	0.6155	722.9
	$N^L = 4$	769	0.3445	1788	0.6160	722.8
	$N^L = 5$	769	0.3448	1782	0.6161	723.6
	$N^L = 1$	1025	0.3448	1878	0.6162	725.9
	$N^L = 2$	1025	0.3426	1876	0.6161	725.4
	$N^L = 3$	1025	0.3428	1867	0.6165	724.9
	$N^L = 4$	1025	0.3429	1866	0.6164	725.2
	$N^L = 5$	1025	0.3429	1871	0.6163	725.3
	Variant I_{LO} [13]	768	0.3414	1898	0.6164	725.2

Table 3: The values of the first two maxima of palinstrophy for Re = 625 and Re = 1250.

Re	Results	K	t_1	$P_1(t_1)$	t_2	$P_2(t_2)$
625	PS	257	0.3629	1.386×10^7	0.6521	6.776×10^5
	PS [19]	256	0.3632	1.386×10^7	0.6521	6.777×10^5
	FD2	257	0.3760	8.113×10^6	0.6817	5.606×10^5
		513	0.3642	1.273×10^7	0.6469	6.549×10^5
		769	0.3625	1.351×10^7	0.6489	6.659×10^5
		1025	0.3625	1.364×10^7	0.6508	6.735×10^5
	FD [19]	1024	0.363	1.296×10^7	0.653	6.561×10^5
	$N^L = 1$	257	0.3764	5.866×10^6	0.7002	7.151×10^5
	$N^L = 2$	257	0.3784	7.972×10^6	0.6759	7.508×10^5
	$N^L = 3$	257	0.3771	9.652×10^6	0.6731	7.221×10^5
	$N^L = 4$	257	0.3750	1.039×10^7	0.6531	7.096×10^5
	$N^L = 5$	257	0.3735	1.027×10^7	0.6580	7.347×10^5
	$N^L = 1$	513	0.3646	1.428×10^7	0.6519	6.884×10^5
	$N^L = 2$	513	0.3642	1.564×10^7	0.6500	6.892×10^5
	$N^L = 3$	513	0.3639	1.561×10^7	0.6511	6.892×10^5
	$N^L = 4$	513	0.3639	1.524×10^7	0.6519	6.880×10^5
	$N^L = 5$	513	0.3642	1.493×10^7	0.6519	6.885×10^5
	$N^L = 1$	769	0.3626	1.437×10^7	0.6516	6.799×10^5
	$N^L = 2$	769	0.3624	1.458×10^7	0.6515	6.791×10^5
	$N^L = 3$	769	0.3625	1.447×10^7	0.6518	6.788×10^5
	$N^L = 4$	769	0.3625	1.445×10^7	0.6517	6.788×10^5
	$N^L = 5$	769	0.3626	1.450×10^7	0.6516	6.788×10^5
	Variant 1_{HO} [13]	512	0.3646	1.519×10^7	0.6558	6.897×10^5
		768	0.3626	1.455×10^7	0.6520	6.789×10^5
		1024	0.3624	1.412×10^7	0.6518	6.775×10^5

The trends observed in Figs. 10 and 11 are quantitatively confirmed by the data reported in Tabs. 2 and 3. For Re = 625, the FD2 scheme exhibits a strong dependence on grid resolution. On the coarsest grid ($K = 257$), both the enstrophy and palinstrophy maxima are substantially underpredicted relative to the PS reference solution. Increasing grid resolution progressively improves the agreement, although accurate prediction of the extrema still requires relatively fine grids.

The ADD-enhanced discretization provides a substantial improvement already on coarse grids. For $K = 513$, the predicted values of the first and second enstrophy maxima are comparable to those obtained using the FD2 scheme on the finer grid with $K = 769$. A further improvement is achieved on the grid with $K = 769$, where all ADD variants predict both enstrophy maxima with an accuracy comparable to that obtained using FD2 on the much finer grid with $K = 1025$. Furthermore, the ADD results obtained on $K = 769$ are more accurate than those reported by Tyliszczak [13] for the Variant 1_{HO} scheme on a comparable grid resolution ($K = 768$), while approaching the accuracy achieved by the same HOCD formulation on the finer grid with $K = 1024$. This result demonstrates that the ADD procedure achieves accuracy comparable to that of established HOCD schemes.

For Re = 1250, a similar trend for enstrophy evolution is observed. Although the differences between the discretization schemes are less pronounced than for Re = 625, the ADD-enhanced discretization consistently improves the prediction of both enstrophy maxima relative to the underlying FD2 scheme. In particular, the results obtained with ADD on $K = 769$ are comparable to those obtained with FD2 on the finer grid with $K = 1025$, while the predictions on $K = 1025$ approach the PS reference solution.

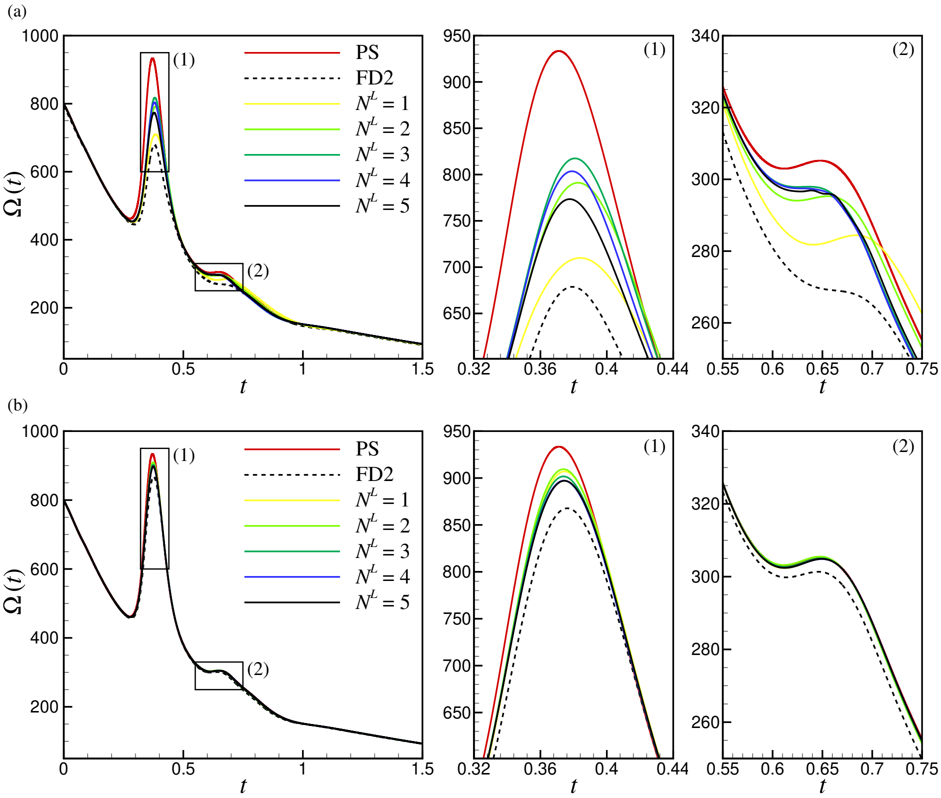

Figure 10: Enstrophy evolution for Re = 625 on grids with $K = 257$ (a) and $K = 513$ (b).

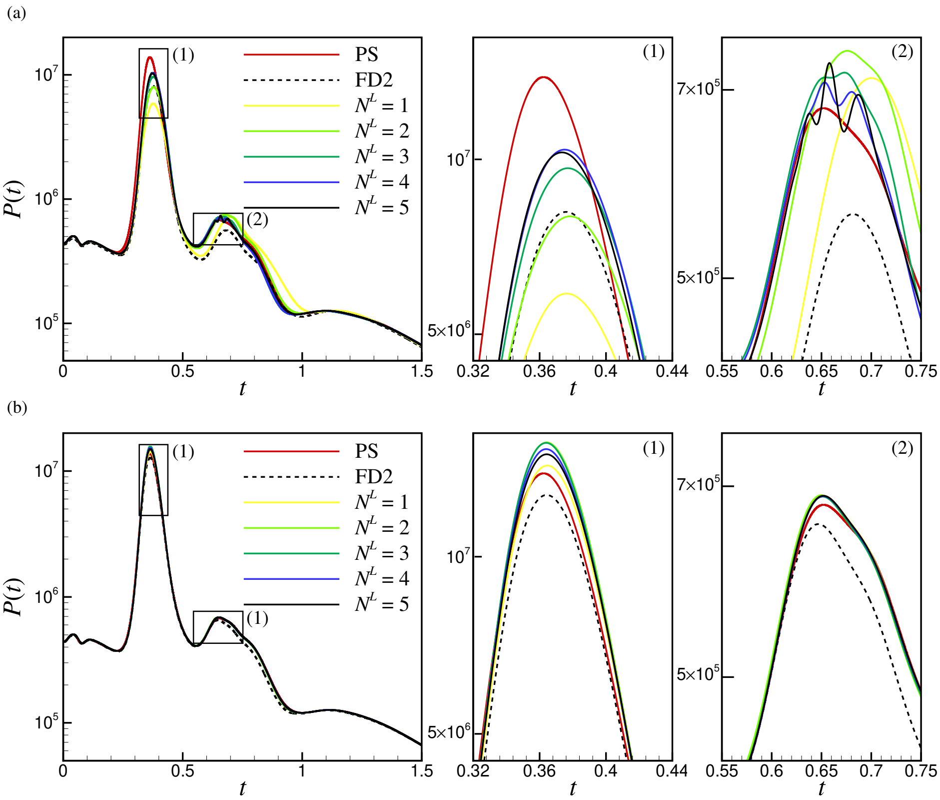

Figure 11: Palinstrophy evolution for Re = 625 on grids with $K = 257$ (a) and $K = 513$ (b).

For palinstrophy (Fig 11), the influence of the ADD procedure is less obvious. Although its second maximum is generally predicted more accurately by ADD than by the classical FD2 scheme, the first maximum tends to be overestimated on finer grids. As in the case of enstrophy, no clear monotonic dependence on N^L is observed.

The lack of a clear ordering with respect to N^L, observed for both Reynolds numbers considered, suggests that overall accuracy is no longer controlled solely by discretization of the first-derivative terms. Since additional computations with smaller time steps produced virtually identical results, the remaining discrepancies are likely due to other components of the solution algorithm, particularly the discretization of the viscous terms. The influence of the discretization of the second-derivative terms on the overall solution accuracy remains the subject of ongoing research.

5.4 Three-dimensional cavity flow

The final benchmark considered in this study is the three-dimensional lid-driven cavity flow, which is commonly used for the verification and validation of numerical methods and algorithms for the incompressible Navier-Stokes equations, see e.g. [20,21]. This is primarily due to the presence of complex three-dimensional flow structures in a geometrically simple configuration and the strong coupling between convection, diffusion, and pressure effects, with significant influence from solid boundaries throughout the entire computational domain. Consequently, the 3D cavity flow provides a demanding test of the proposed ADD methodology in a fully three-dimensional wall-bounded flow.

The computations are performed in a cubic cavity of dimensions $L_x = L_y = L_z = 1$. All boundaries are treated as no-slip walls. The upper wall moves with a constant velocity $u_1 = 1$ in the x-direction, while the remaining walls are stationary. The simulations are performed using the velocity–pressure formulation implemented in the in-house SAILOR solver, as described in Section 4.2. The ADD procedure is applied exclusively to the first-derivative operator appearing in the convective terms, whereas the second-derivative operator and other first-order derivatives are discretized using different order finite and compact difference schemes, as discussed in Section 4.2. The performance of both ADD variants introduced in Section 3 is examined through comparisons with solutions obtained using the tenth-order compact difference method (CD10) validated against literature data.

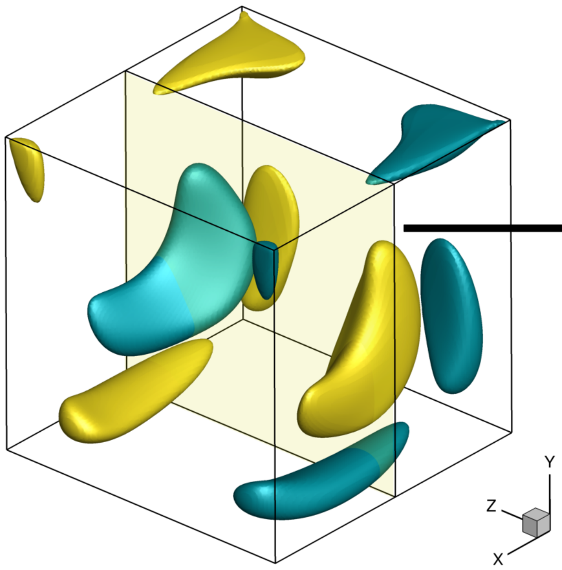

(a)

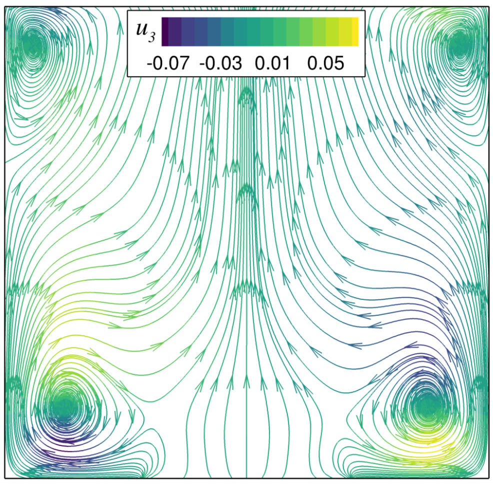

(b)

Figure 12: 3D cavity flow at Re = 1000: iso-surfaces of $u_3 = 0.035$ (yellow) and $u_3 = -0.035$ (blue) (a), and streamlines in the central plane ($x = 0$) colored by u_3 (b).

Figure 12 presents representative flow structures obtained for Re = 1000. The iso-surfaces of the velocity component u_3 corresponding to $u_3 = 0.035$ (yellow) and $u_3 = -0.035$ (blue), shown in Fig. 12a, illustrate the three-dimensional nature of the flow. The light-yellow plane indicates the central cavity plane ($x = 0$), whose detailed view is presented in Fig. 12b. The streamlines shown in Fig. 12b reveal four counter-rotating corner vortices and confirm that the solution remains symmetric with respect to the cavity centerline, consistent with previous studies [20, 21].

To validate the numerical implementation, selected velocity profiles are compared with the reference pseudo-spectral (PS) solutions reported by Ku et al. [20]. The present CD10 computations were performed on grids with $K = 65$ and $K = 129$. Since both resolutions produced nearly identical velocity profiles, only the results obtained on the finer grid ($K = 129$) are shown in Figure 13 and used as the reference solution in the subsequent assessment of the ADD methodology. Figure 13a shows the horizontal velocity component u_1 obtained using CD10 scheme and sampled along the vertical centerline ($x = 0$) for Re = 100 and Re = 1000, while Fig. 13b shows the corresponding profiles of the vertical component u_2 along the horizontal centerline ($y = 0$) for the same Reynolds numbers. Excellent agreement between the present CD10 solution and the reference PS data is observed. These results demonstrate that the SAILOR code accurately reproduces the benchmark solution for the 3D lid-driven cavity flow.

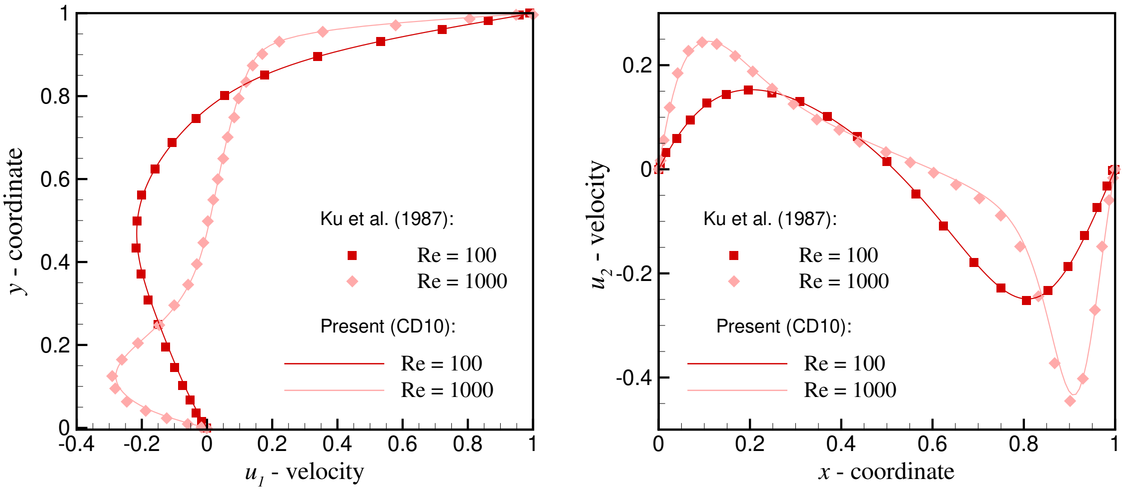

(a) (b)

Figure 13: 3D cavity flow: comparison of the present CD10 results with the PS solutions of Ku et al. [20] for Re = 100 and Re = 1000. Profiles of u_1 along $x = 0$ (a) and u_2 along $y = 0$ (b),

Figure 14 illustrates the effect of the ADD procedure on the prediction of the u_2 velocity profile at Re = 1000. All FD2 and ADD results shown in this figure were obtained on the grid with $K = 65$, while the reference CD10 solution was computed on the finer grid with $K = 129$. The FD2 discretization exhibits the largest deviations from the reference profile, particularly in the vicinity of the local maximum and minimum marked as points (1) and (2), respectively. The application of the ADD substantially improves the prediction of both extrema, bringing the solution significantly closer to the CD10 reference profile (see enlarged views). Only minor differences between the standard and stabilized ADD formulations are observed in this test case. Although the stabilized formulation slightly reduces the magnitude of the recovered extrema, the differences remain small compared to the improvement achieved relative to the underlying FD2 discretization. Moreover, in this flow problem the stabilized formulation preserves most of the accuracy benefits provided by ADD while ensuring computational stability.

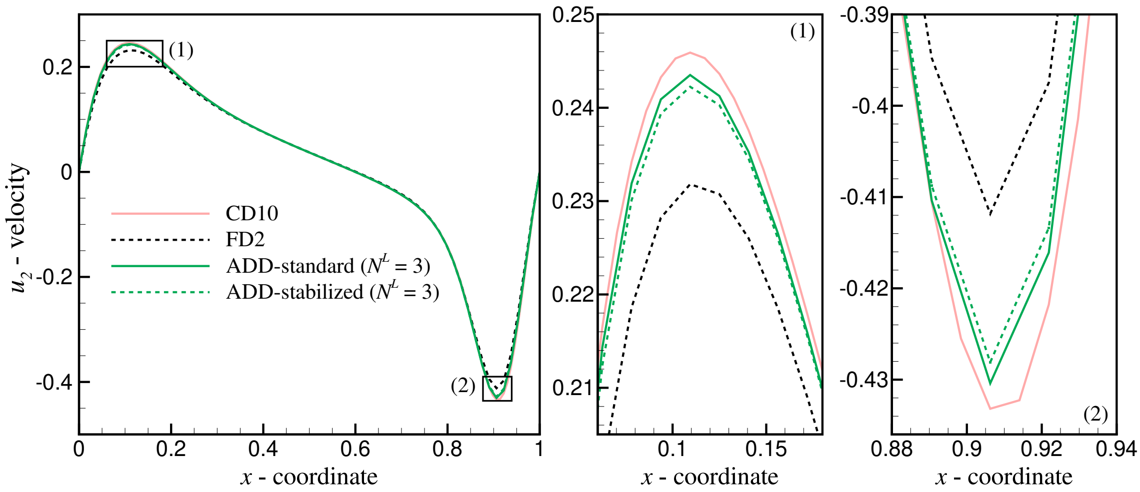

Figure 14: 3D cavity flow at Re = 1000: comparison of the FD2 and ADD-enhanced discretizations against the CD10 reference solution. Profiles of u_2 along $y = 0$.

6. Conclusions and Future Work

The present work extended the Approximate Deconvolution Discretization (ADD) framework to non-periodic domains through the construction of boundary-aware induced filters and the corresponding approximate deconvolution operators. The proposed formulation removes one of the principal limitations of the original ADD methodology proposed in [4], enabling its application to flow configurations involving physically relevant boundary conditions. Furthermore, a general procedure for constructing induced filters in the presence of physical boundaries has been developed, providing a mathematical framework that goes beyond the FD2 discretization considered here and establishes a foundation for future extensions of ADD to other classes of CFD discretizations.

A spectral analysis of the resulting ADD operators revealed that the extension to non-periodic domains may introduce unstable eigenmodes associated with the boundary treatment. To address this issue, a stabilized formulation was proposed in which the deconvolution procedure is locally disabled near physical boundaries. The analysis demonstrated that this modification effectively removes the unstable modes and restores the stability of the corresponding semi-discrete operators. At the same time, the numerical experiments showed that the influence of this stabilization strategy on the overall solution accuracy is strongly problem-dependent and depends on the role of near-boundary dynamics in the considered flow configuration.

The benchmark hierarchy revealed a progressive change in the factors controlling the overall accuracy of the solution. For the inviscid vortex advection problem, where boundary effects and viscous terms are absent, increasing the interpolation stencil N^L resulted in systematic accuracy improvements confirming the ability of the ADD procedure to compensate for discretization-induced filtering errors. For the Burggraf flow, the influence of wall boundary conditions reduced this monotonic behavior and highlighted the importance of near-wall regions for the effectiveness of the deconvolution procedure. In the dipole-wall interaction benchmark, additional error sources associated with viscous effects, vortex-wall interactions and the generation of increasingly complex small-scale structures further limited the benefits of improving the first-derivative approximation alone.

Despite these increasing challenges, the ADD-enhanced discretizations consistently outperformed the underlying FD2 scheme in all benchmark problems considered. In the inviscid vortex advection problem, ADD produced substantial reductions of the numerical error relative to the baseline discretization. For the Burggraf flow, accuracy improvements of several orders of magnitude were obtained whenever the solution remained stable. In the dipole-wall interaction benchmark, the ADD-enhanced discretizations provided significantly more accurate predictions of enstrophy and palinstrophy extrema than the underlying FD2 formulation and achieved an accuracy level comparable to that of established high-order compact difference methods (HOCD). In selected cases, the ADD results obtained on relatively coarse grids approached or exceeded the accuracy reported for HOCD discretizations on comparable resolutions.

The successful application of ADD to the three-dimensional lid-driven cavity flow further suggests that the proposed methodology remains effective beyond the two-dimensional benchmark configurations considered in the present study and provides a promising basis for future applications to increasingly complex three-dimensional CFD simulations.

The results demonstrate that ADD offers an alternative route toward high-accuracy CFD simulations that differs fundamentally from the traditional strategy of increasing the formal order of discretization. Rather than achieving higher accuracy through increasingly sophisticated discretization schemes, the proposed methodology improves solution accuracy through the recovery of scales attenuated by discretization-induced filtering. More generally, the present extension represents a step toward establishing ADD as a generic accuracy-enhancement framework for CFD discretizations in complex geometries and non-periodic domains. Future work will focus on further developing the mathematical foundations of ADD and exploring its applicability across a broader range of CFD discretization frameworks and flow regimes.

Acknowledgements

This work was supported by statutory funds of the Czestochowa University of Technology (BS/PB 1-100-301/2026/P). The authors gratefully acknowledge the high-performance infrastructure PLGrid ACK Cyfronet AGH and PCSS (Poland), and SURF (The Netherlands) for providing computer facilities and support within computational grants no. PLG/2025/018864, PL0356-01, and NWO-2024.016 (Snellius supercomputer) - Multiscale Modeling and Simulation.

References

[1] Rogallo R. S., Moin P. Numerical Simulation of Turbulent Flows. *Annual Review of Fluid Mechanics*, 16(1):99–137, 1984.

[2] Geurts B.J, van der Bos F. Numerically induced high-pass dynamics in large-eddy simulation. *Physics of Fluids*, 17(12):125103, 2005.

[3] Caban L., Tyliszczak A., Geurts B. J. Analysis of the impact of numerically induced high-order filters and regularization on LES modelling of an incompressible 3D Taylor-Green vortex flow undergoing laminar-turbulent transition. *Computers & Fluids*, 312:107015, 2026.

[4] Boguslawski A., Tyliszczak A., Geurts B.J. Approximate Deconvolution Discretisation. *Computers and Mathematics with Applications*, 154:175–198, 2024.

[5] van Cittert P.H. Zum Einfluß der Spaltbreite auf die Intensitätsverteilung in Spektrallinien. II. *Zeitschrift für Physik*, 69:298–308, 1931.

[6] Caban L., Tyliszczak A., Abide S., Domaradzki J. A. A very high-order compact difference methodfor wall-bounded flows. *AIP Conference Proceedings, AIP Publishing LLC*, 3094:500008, 2024.

[7] Gustafsson B., Kreiss H.-O., Oliger J. *Time-Dependent Problems and Difference Methods*. John Wiley & Sons, Inc., 1995.

[8] Carpenter M. H., Gottlieb D., Abarbanel S. Stable and accurate boundary treatments for compact, high-order finite-difference schemes. *Applied Numerical Mathematics*, 12:55–87, 1993.

[9] Svärd M., Nordström J. On the order of accuracy for difference approximations of initial-boundary value problems. *Journal of Computational Physics*, 218:333–352, 2006.

[10] Claudio Canuto, M.Yousuff Hussaini, Alfio Quarteroni, Thomas A., Jr. Zang. *Spectral Methods in*

Fluid Dynamics. Springer-Verlag, 1988.

[11] Lynch R.E., Rice J.R., Thomas D.H. Direct solution of partial difference equations by tensor product methods. *Numerische Mathematik*, 6:185–199, 1964.

[12] Fletcher, C. A. J. *Computational Techniques for Fluid Dynamics*. Springer-Verlag, 1991.

[13] Tyliszczak, A. A high-order compact difference algorithm for half-staggered grids for laminar and turbulent incompressible flows. *Journal of Computational Physics*, 276:438–467, 2014.

[14] Fortin M., Peyret R., Temam R. Résolution numérique des équations de Navier–Stokes pour un fluide incompressible. *Journal de Mécanique*, 10(3):357–390, 1971.

[15] Knikker, R. Study of a staggered fourth-order compact scheme for unsteady incompressible viscous flows. *International Journal for Numerical Methods in Fluids* , 59:1063–1092, 2009.

[16] Caban L., Tyliszczak A. High-order compact difference schemes on wide computational stencils with a spectral-like accuracy. *Computers and Mathematics with Applications*, 108:123–140, 2022.

[17] Laizet S., Lamballais E. High-order compact schemes for incompressible flows: A simple and efficient method with quasi-spectral accuracy. *Journal of Computational Physics*, 228(16):5989–6015, 2009.

[18] Patankar, S. V. *Numerical Heat Transfer and Fluid Flow*. Taylor and Francis, 1980.

[19] Clercx H. J. H., Bruneau C.-H. The normal and oblique collision of a dipole with a no-slip boundary. *Computers & Fluids*, 35:245–279, 2006.

[20] Ku H. C., Hirsh R. S., Taylor T. D. A pseudospectral method for solution of the three-dimensional incompressible Navier–Stokes equations. *Journal of Computational Physics*, 70:439–462, 1987.

[21] Tyliszczak A., Deconinck H. Application of time preconditioning and high-order compact discretization method for low Mach number flows. *International Journal for Numerical Methods in Fluids*, 72(6):650–670, 2013.